Balloon seismology enables subsurface imaging without ground stations

Marouchka Froment[1*], Quentin Brissaud[1], Sven Peter Näsholm[1,2], Johannes Schweitzer[1,3]

[1]Solutions Department, NORSAR, Gunnar Randers vei 15, Kjeller, 2007, Norway.
[2]Department of Informatics, University of Oslo, Gaustadalléen 23B, Oslo, 0373, Norway.
[3]Centre for Planetary Habitability (PHAB), University of Oslo, Sem Sælands vei 1, Oslo, 0371, Norway.

*Corresponding author(s). E-mail(s): marouchka.froment@norsar.no;

Abstract

Knowledge of the seismic velocity structure provides essential insights into the composition and evolution of planetary interiors. The Earth's structure is primarily derived from the inversion of seismic signals recorded by seismometers at the ground. However, on Venus, harsh surface conditions prevent the deployment of ground-based instruments. Ballon-borne seismology provides an alternative by recording the low-frequency acoustic wave signature of seismic waves, known as infrasound, from the high atmosphere. Here, we show that seismic velocities and earthquake source location can be jointly inverted from such balloon observations. We demonstrate this method using infrasound signals recorded by a network of four stratospheric balloons following a major earthquake in the Flores Sea, Indonesia. We implement a Bayesian inversion using Markov chain Monte Carlo sampling, allowing us to assess trade-offs inherent to the joint location and velocity estimation. The distributions of source location and seismic velocity structure are consistent with results obtained using ground seismometers in terms of mean and uncertainty. Our ability to estimate source and velocity parameters without ground deployments paves the way for the development of future seismo-acoustic missions to Venus, and provides new opportunities for seismic exploration in Earth remote regions.

1 Introduction

Exploring the interior of Venus could yield crucial insights into its evolution and current geodynamic regime, which remain unknown (Rolf et al. 2022). The global network of seismometers on Earth's surface was crucial to developing 1D models of Earth's interior (e.g., Dziewonski and Anderson (1981); Kennett and Engdahl (1991);

Kustowski et al. (2008)) , and now contributes to revealing 3D heterogeneities in the mantle and crust (see e.g., (Tromp 2020; Berg et al. 2020)). Beyond Earth, successful seismometer deployments on Mars and the Moon have provided invaluable information about their structure (Latham et al. 1969; Banerdt et al. 2020) and new seismology missions are now planned to explore Titan (Lorenz et al. 2019; Panning et al. 2020; Lorenz et al. 2021). However, surface deployment remains challenging on Venus due to the short lifespan of electronics at its high surface temperature (~ 460 K) (Stevenson et al. 2015; Garcia et al. 2024).

In recent years, new key observations have demonstrated the potential of balloon-borne microbarometers to detect the acoustic signature of seismic waves (Krishnamoorthy et al. 2018, 2019; Garcia et al. 2021). These new observations emerge from the mechanical coupling of seismic ground motion into infrasound – acoustic waves below ~ 20 Hz, due to stress continuity at the surface (Mutschlecner and Whitaker 2005; Brissaud et al. 2017). Due to the large velocity contrast between a planet and its atmosphere and low attenuation at low frequencies, seismic waves generate vertically-propagating acoustic waves with dispersion characteristics similar to those of their seismic counterparts (Brissaud et al. 2021). Importantly, this coupling is expected to be two orders of magnitude stronger on Venus due to its dense atmosphere (Lognonné and Johnson 2015; Averbuch et al. 2023), enabling the detection of converted seismic waves across a wide range of altitudes. Ballon platforms are therefore considered a realistic alternative to ground deployments to explore Venus' interior (Stevenson et al. 2015; Didion et al. 2018; Sutin et al. 2018; Garcia et al. 2024). They offer several advantages for subsurface monitoring, such as their mobility and ability to survey large areas. On Venus, balloons operate under acceptable pressure and temperature conditions above 40 km and were successfully deployed during the Soviet VEGA missions (Linkin et al. 1986). They are also relatively inexpensive and benefit from recent advances enabling long-duration controlled flights (Schuler et al. 2022; Bellemare et al. 2020).

The recent recordings of earthquake infrasound on Earth therefore represent a unique opportunity to assess the use of balloon infrasound for seismic source localization and subsurface exploration. Brissaud et al. (2021) detected a magnitude 4.2 aftershock using free-floating balloons following the July 2019 Ridgecrest earthquake. However, signals were only recorded at one balloon, did not show body wave arrivals, and surface wave signals had a low Signal-to-Noise Ratio (SNR) which prevents the joint inversion of source and subsurface properties. A year later, Garcia et al. (2022) reported the detection of a Mw 7.5 earthquake in Peru and a Mw 7.3 earthquake in the Flores Sea using freely floating stratospheric balloons from the Strateole2 campaign (Haase et al. 2018). In particular, infrasound from the Flores Sea earthquake was recorded by four balloons at large SNRs. Garcia et al. (2022) showed excellent agreement between balloon pressure signals and ground-based vertical velocity records. Recently, Gerier et al. (2024) modeled this event numerically, including atmospheric coupling, and demonstrated that major seismic phases – P and S body waves and

Rayleigh surface waves (LR) – are identifiable in the balloon data. However, it is still largely unknown how accurately such waveforms can provide insights into seismic sources and seismic velocity models.

In this contribution, we show that body- and Rayleigh-wave arrival times at various frequencies are sufficient to constrain these seismic parameters through a Bayesian inversion approach, even with a small number of balloon stations. We apply this inversion to retrieve the hypocenter of the 2021 M_w 7.3 Flores Sea earthquake and a 1D model of subsurface seismic velocities in the region. The inversion is first tested using P, S, and LR arrivals identified at ground stations, and then using arrivals identified in Strateole2 balloon recordings. We finally quantify the uncertainty in the retrieved source location and seismic velocities.

2 Results

2.1 A joint Inversion model for source and subsurface parameters

Due to the absence of strong acoustic dispersion at low frequencies in Earth's atmosphere, earthquake-induced infrasound signals are scaled images of the vertical ground velocity at the surface below the balloon (Garcia et al. 2022; Macpherson et al. 2023). A forward model of arrival times at balloon platforms can thus be readily derived from classical seismological methods. Consequently, we use both body- and surface-wave arrival times in several frequency bands to retrieve the source and subsurface parameters. Relying on arrival times instead of full waveform modelling eliminates the need for an accurate source model and the reliance on low-frequency waveforms, which are typically contaminated by buoyancy oscillations and turbulence in balloon data (Massman 1978; Garcia et al. 2022).

For planetary exploration, joint subsurface and source inversion is required due to our lack of prior knowledge on subsurface structures and source locations. Additionally, the sparsity of balloon networks on Earth, and possibly on Venus, calls for careful assessment of uncertainty in hypocenter coordinates (Arrowsmith et al. 2020). To solve the ill-posed hypocenter-velocity problem (Thurber 1992), we employ a Bayesian approach, which performs a global search through model space using a Markov Chain Monte Carlo (MCMC) method (see, e.g., the monograph by Tarantola (2005)). This approach combines the misfit between predicted and observed arrival times (likelihood) with the provided prior information for each inverted parameter (prior) to infer the probability distribution for these parameters (posterior). The present McMC inversion is adapted from the Ensemble Sampler (Goodman and Weare 2010; Foreman-Mackey et al. 2013).

The inverted source variables are origin time t_s, source latitude and longitude, and depth (lon_s, lat_s, h_s). The subsurface is modeled as six homogeneous layers over a halfspace, and the shear wave velocity $v_{S,i}$, Poisson's ratio ν_i and thickness H_i of each layer i are inverted. Prior ranges for these variables are described in the Methods and Extended Table A1.

2.2 The 2021 Flores earthquake

The Flores Sea earthquake occurred on December 14, 2021, with a magnitude of 7.3. Following relocation, Supendi et al. (2022) associate the event with the Kalaotoa fault system, identifying a strike-slip mechanism at a depth of 12.2 km. This aligns with USGS estimates of 14.2 km based on source location and 17.5 km from moment tensor inversions (International Seismological Center 2025).

Few subsurface velocity models have been proposed near the Flores Sea, a region characterized by high heterogeneity due to the presence of several subduction zones. To provide a meaningful reference for the interpretation of inverted subsurface models, we define a Median Model based on the median of CRUST1.0 models (Laske et al. 2013) and LLNL-G3D-JPS tomographic models in the mantle (Simmons et al. 2015) below our stations (see Supplementary Figures S4 and S5). In our comparisons, we consider 15 km depth, latitude $-7.6°$N and longitude 122.2°E as the reference hypocenter (USGS CMT solution, International Seismological Center (2025)), and 03:20:23 UTC as the reference origin time.

At the time of the event, four Strateole2 balloons, identified as TTL4-07, TTL4-15, TTL5-16 and TTL3-17, were located between 680 and 2800 km to the northeast of the event. The balloon inversion uses body and surface wave arrival times extracted from their pressure traces. The SNR of the Strateole2 pressure data is low at long periods due to the presence of the balloon buoyancy resonance (Massman 1978). These oscillations were partly corrected using a method similar to Podglajen et al. (2022) (see Methods and Extended Figure A1 for details). P-wave arrival times were picked for the four balloons with a measured uncertainty between 7 and 35 s, and S wave arrivals with uncertainties between 8 and 49 s. Due to low-frequency noise, the LR arrival could only be identified with confidence for TTL3-17 and TTL5-16 between 0.005 and 0.1 Hz, with a mean uncertainty of around 50 s. The picks are shown in Fig. 3 and in more details in the Supplementary Figures S2 and S3.

In order to assess the robustness of this infrasound-based inversion, we also construct a reference source and subsurface model through the inversion of data recorded at 11 seismic stations selected among the Global Seismograph Network, the Australian National Seismograph Network, and the German GEOFON seismic network. This separate inversion allows us to build confidence in the joint inversion technique, and to compare the resolution obtained from a small number of receivers at low SNR – the balloon case – to the one obtained from a typical dense ground network of receivers at high SNR – the seismic case. For consistency, we pick the seismic arrivals using vertical velocity signals from seismic stations in the Flores region, simulating a single-component infrasound signal. The 11 chosen stations are illustrated in Fig. 1a and detailed in Supplementary Table S1. For these stations, uncertainty of the P wave

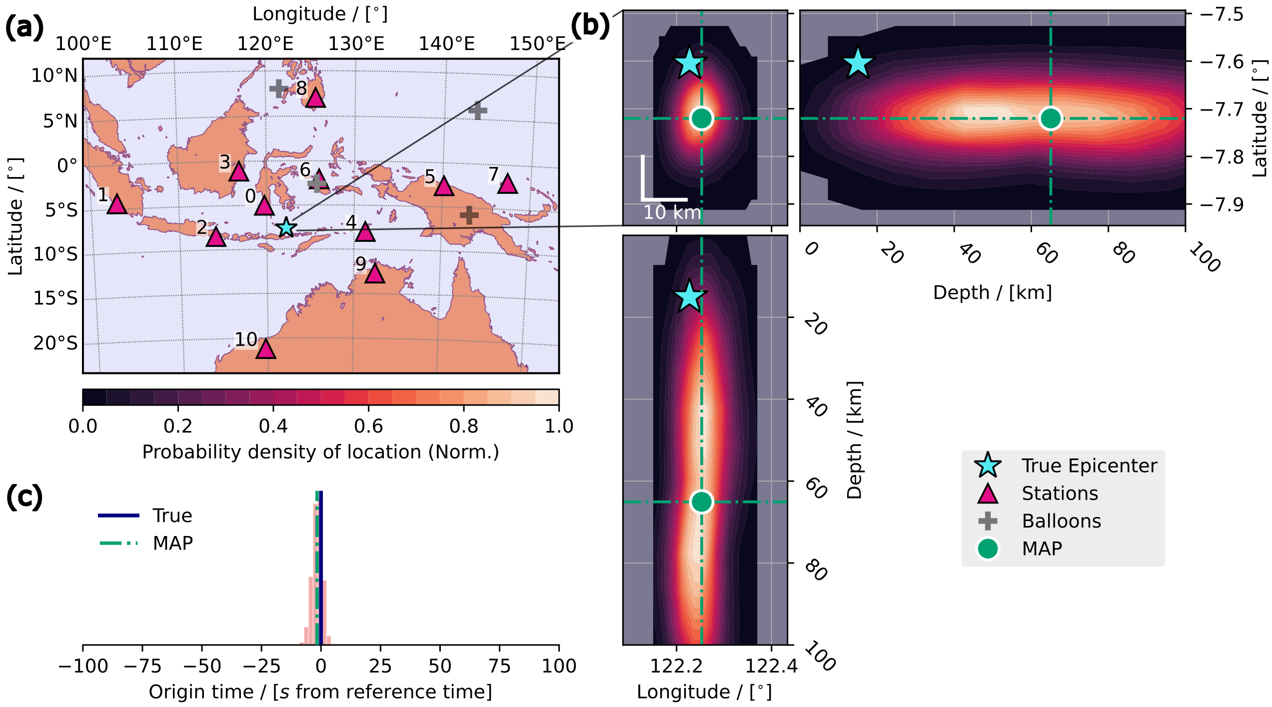

Fig. 1 Source origin inverted using 11 seismic stations. (a) Map of chosen ground seismic stations for the inversion of the 2021 Mw 7.3 Flores earthquake. The four Strateole2 balloons are marked with gray crosses for comparison. Plot (b) shows the marginal distribution of the source hypocenter, up to scale between horizontal and vertical slices. (c) shows the histogram of source origin time, centered around the true value of zero, with the MAP solution in green.

arrival times ranged between 1 and 2 s, 10 to 40 s for S waves, and 20 to 100 s for LRs between 0.002 and 0.2 Hz.

2.3 Source and subsurface as seen from seismic data

The joint inversion is first performed using picks obtained from 11 seismic stations. The McMC simulations return an ensemble of source and subsurface parameters forming the posterior probability distribution. To interpret these results, we reduce the dimensions of the posterior by calculating marginal distributions, and by estimating the Maximum A Posteriori (MAP) parameters, i.e. the solution maximizing the posterior distribution function (see Methods and Supplementary Table S2).

The marginal distribution of source parameters inverted from these arrival times is shown in Fig. 1b. The MAP source location is shifted 13 km south of the true epicenter, at a slightly larger distance to the majority of the stations, which are to the north. This longer travel time is accommodated by a slightly earlier source origin time, with the MAP value 2 ± 2 s earlier than the reference time (1c). The inversion also favors a source about 50 km deeper than the reference solution, with 100 km uncertainty. The marginal distributions of source parameters follow Gaussian distributions with little trade-offs between variables.

Fig. 2 displays the marginal posterior distributions for the shear wave velocity v_S and the Poisson's ratio ν as function of depth. Both ν and v_s appear constrained down to ~ 500 km depth. The MAP models are in good agreement with the Median profile, constructed from global tomographic Earth models, especially for the shear wave velocity. Posterior values of v_S have a $1-\sigma$ uncertainty of ± 0.1 km/s in the crust and upper mantle layers, and ± 0.6 km/s in the top sediment layer. It is the least well defined, likely due to the high variability of LR dispersion above 0.1 Hz (Fig. 2a). The $1-\sigma$ uncertainty becomes 0.5 to 0.6 km/s in the lowermost layer and halfspace (Fig. 2c). The Poisson's ratio takes values between 0.21 and 0.29, within the range expected for most minerals (Christensen 1996). It is constrained with an large uncertainty of ± 0.02 between 100 and 400 km depth, and is otherwise undefined.

The inversion method also returns a distribution of layer thicknesses, which can be converted to a more easily interpretable distribution of interface depths through cumulative summation. In Fig. 2c and 2f, we compare the posterior distribution of interfaces to the prior, thereby highlighting which depth ranges have a higher probability of hosting a change in subsurface properties, independently from the prior model

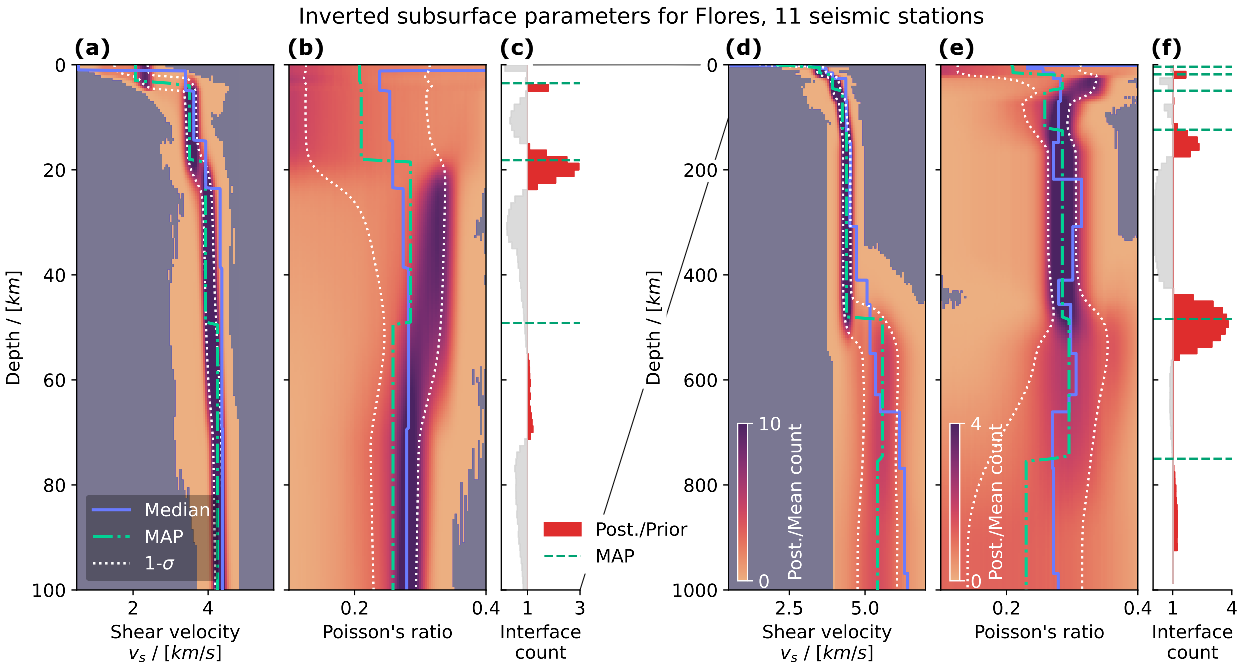

Fig. 2 Subsurface velocity model inversion results using 11 seismic stations. Models for shear wave velocity v_s and Poisson's ratio ν below the Flores Sea, inverted using 11 local seismic station. Models down to 100 km are shown in (a) and (b) and to 1000 km in (d) and (e). The Median literature model is shown in blue, the MAP in green and the $1-\sigma$ probability region in dashed white lines. Red histograms in panels of (c) and (f) represent regions with a high probability of presenting an interface, or strong gradient in subsurface properties (see the Methods section for details on this metric), together with the MAP interfaces in green.

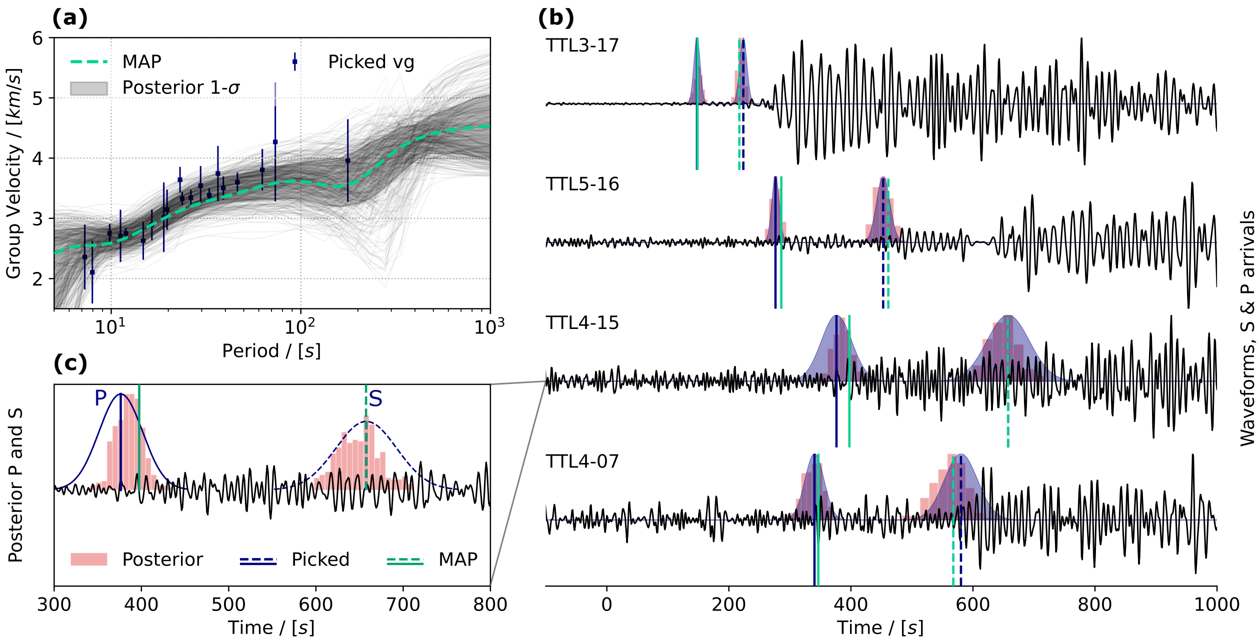

Fig. 3 Infrasound signals and arrivals at balloons following the M_w 7.3 Flores earthquake, compared to arrivals predicted from inverted models. (a) Picked Rayleigh wave group velocities, derived from picked arrival times assuming the true location and time of the Mw 7.3 Flores earthquake, shown in blue. These measurements are compared to 400 group velocity curves constructed from a random selection of posterior models. The MAP model is shown in green. (b) Pressure waveforms used to pick arrivals, bandpass-filtered between 0.06 and 0.2 Hz, with picked times shown in blue and arrival times predicted from the MAP in green. (c) Zoom on TTL4-15 signal, showing the posterior distribution of arrival times for P and S waves compared to the picked value and its uncertainty in blue.

distribution. Three interfaces, or regions of strong velocity gradients, are strongly suggested in our model: at 20 ± 4 km depth in the crust, and 150 ± 30 km, and 500 ± 70 km depth in the mantle. A very shallow interface is also suggested at 4 km depth.

2.4 Source and subsurface inverted from a network of four balloons

The balloon inversion fits the arrival times adequately, as evidenced by the strong match between the observed and posterior distribution of arrivals in Fig. 3. The low number of arrival-times picked from the balloon data, combined with their large uncertainty, limits the precision of the source location. Indeed, Figs. 4a and 4b show a larger uncertainty in epicenter using the Strateole2 balloons, rather than a subset of 4 seismic regional stations at similar locations with more precise P, S and LR picks. The Strateole2 data inversion returns a MAP epicenter 35 km away from the true epicenter at coordinates $-7.5 \pm 1.0°$ latitude and $122.5 \pm 0.7°$ longitude, against 32 km distance with an uncertainty of $\pm 0.6 - 0.8°$ in latitude and longitude using 4 seismic stations. This corresponds to an uncertainty of 200 km around the true epicenter. Still, despite

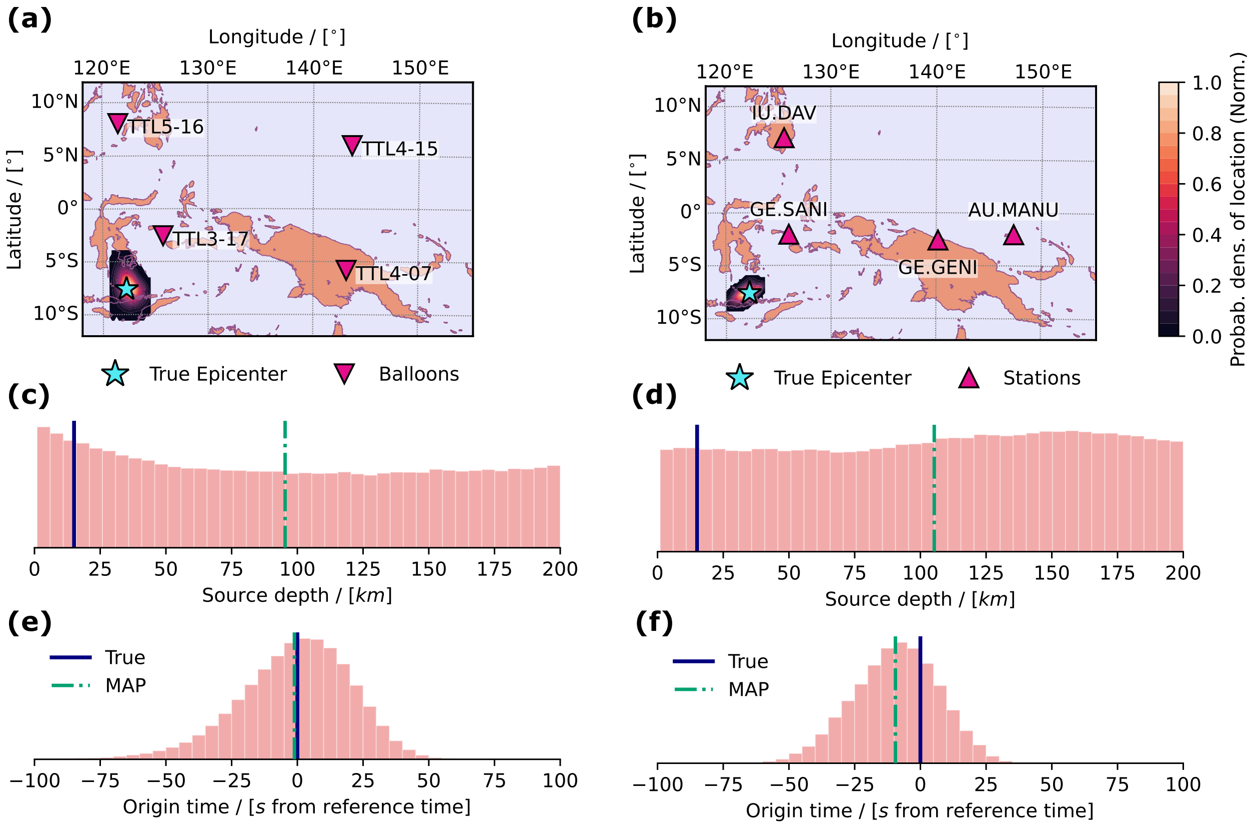

Fig. 4 Source origin inverted from 4 balloon or 4 seismic stations. Posterior distributions of source location (a), depth (c) and origin time (e) inverted from four Strateole2 balloons and (resp. (b), (d), (f)) four seismic stations at similar locations. The true (resp. MAP) values are shown with blue (resp. green) vertical lines.

the low SNR of balloon infrasound signals, the inversion framework enables an accurate characterization of the source location – a critical task when the network is sparse or poorly distributed in terms of source-station azimuth (Arrowsmith et al. 2020).

The origin time is about 1 ± 22 s earlier than the published value for the balloon inversion (Fig. 4e), while it is predicted at -9 ± 16 s using 4 local seismic stations (Fig. 4f). This better result could be due to the slightly wider distribution of balloon stations over azimuth and distance compared to the local ground stations, compensating the imprecision in the picks; or to a biased pick among the ground stations. In both cases, the source depth displays an almost uniform posterior distribution down to 200 km depth and cannot be constrained (Figs. 4c and 4d). Similarly, the 11-station inversion returned a MAP depth of $\sim 40 - 50$ km (Fig. 1b) rather than the 12.2 to 17.5 km previously published (International Seismological Center 2025; Supendi et al. 2022). Inverting source depth without stations close to the source (less than a few source depths away) or identified depth phases is notoriously difficult, making this result unsurprising (Husen and Hardebeck 2010).

With only four P-wave picks, the Strateole2 data insufficiently constrains the Poisson's ratio in the subsurface, where both posterior distributions of ν or v_P are hardly distinguishable from uniform priors (shown in Fig. S10 of the Supplementary Information). However, P, S and LR picks provide constraints on the posterior distribution of v_S, which is shown on Fig. 5a and 5c. The MAP and posterior models matches the Median Model within one standard deviation down to around 600 km depth, and shear wave velocities are constrained with a $1-\sigma$ uncertainty of ±0.3 to ±0.6 km/s between 10 and 400 km depth.

Once again, the interface count metric evaluated from the posterior distribution favors changes in subsurface properties at specific depth ranges, in particular at 19 ± 6 km depth in the crust (see Fig. 5b), a value similar to the 11-station inversion. The Crust1.0 model predicts high variability of crustal thickness in the Malay Archipelago, ranging between 10 km and 43 km at different stations (see Supplementary Figure S5). Thus, the distribution of inverted interfaces likely represents the average Moho depth around the Flores Sea event.

Three deep regions of velocity change are hinted at 420 ± 50 km depth, between 60 and 200 km and below 800 km depth, although with little confidence (Fig. 5d). These values are similar to those found in the 11-station inversion, at 150 ± 30 km and 500 ± 70 km. No global mantle interface is known between 60 and 200 km depth. The wide uncertainty in inverted depth suggests that the high interface probability may not indicate an abrupt change in thermochemical properties, but rather a smooth increase in velocity, as expected at the top of the mantle. Meanwhile, significant velocity changes are know to occur in the mantle transition zone, such as at 410 km depth where the olivine-Wadsleyite phase transition takes place (Helffrich 2000). However, both inverted interface distributions show large uncertainties below 400 km, due to the low sensitivity of P, S, and LR travel times to changes at these depths (see Supplementary Figure S6 and S7). Thus, this concentration of interfaces could rather indicate that a gradual increase in seismic velocity is necessary in this mantle region to fit LR arrival times in the $0.002 - 0.005$ Hz range.

The McMC results also allow for an analysis of trade-offs between inverted parameter in the context of the hypocenter-velocity problem. Fig. 6 represents the marginal posterior probability densities of several inverted variables along one and two dimensions. Trade-offs are observed between the origin time t_s and the source epicenter defined by (lon_s, lat_s) (Fig. 6a and 6b). Regarding the subsurface, complex, non-linear trade-offs exist between the thickness of layers and their seismic velocities (Fig. 6c and 6d). This is a known phenomenon, due to the fact that Rayleigh waves group velocities are sensitive to seismic velocities over a range of depths (see Supplementary Figure S7). Finally, there also exist trade-offs between the Poisson's ratio, which for the balloon inversion is weakly resolved between 0.1 and 0.4, and the shear wave velocity in the same layer (Fig. 6e), and between shear wave velocities in adjacent layers (Fig. 6f). These trade-offs mean that a large number of solution exist for the

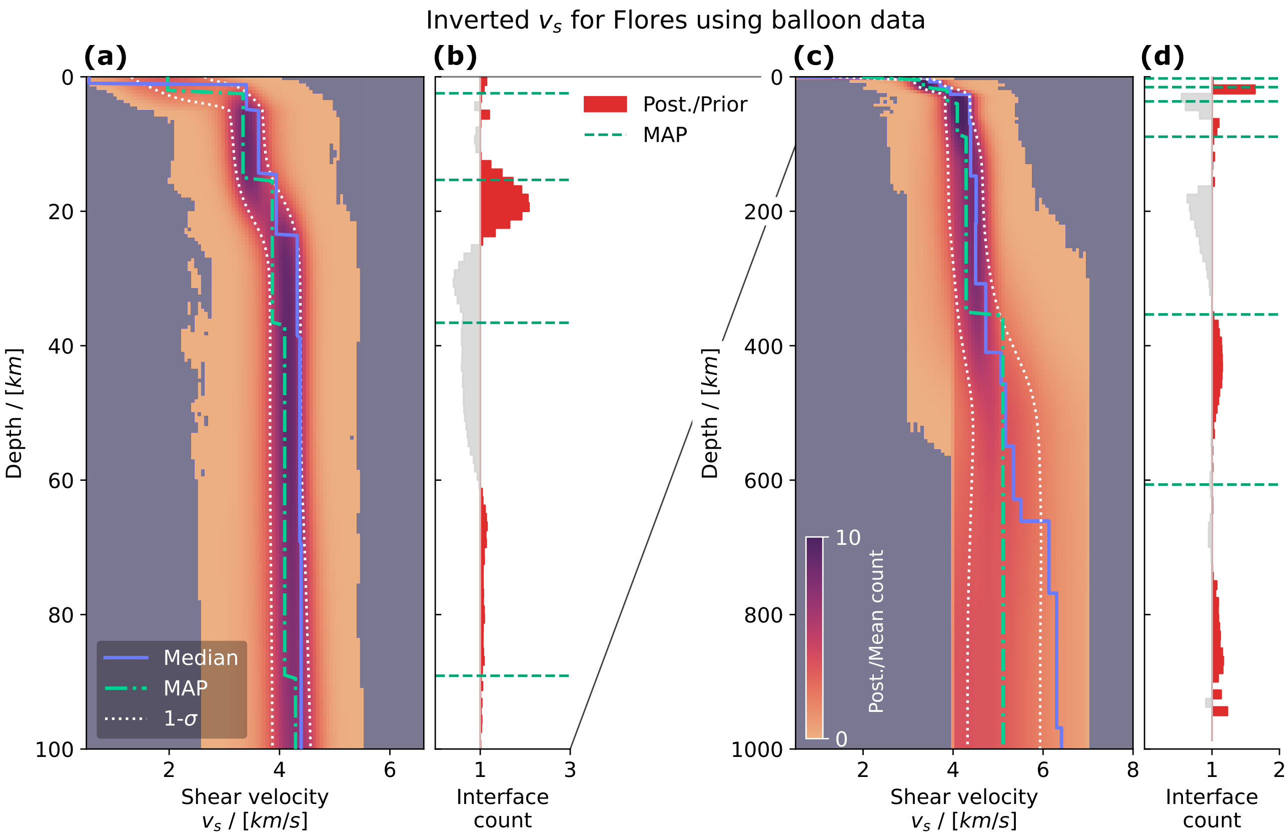

Fig. 5 Subsurface velocity model inverted using Strateole2 infrasound data. Shear wave velocities inverted from balloon data, down to 100 km (a) and 1000 km depth (c), along with the associated ratio of posterior and prior interface depth distributions ((b) and (d), resp.). The MAP model and interface depths are shown in green, and the Median literature model in blue, along with the $1-\sigma$ probability region in dashed white lines.

non-linear, ill-defined system of equations defining arrival times (Methods, Eqs. 1). Yet, our probabilistic inversion framework still highlights regions of higher probability for source location and subsurface properties.

3 Perspectives for balloon seismology

We achieve the inversion of a subsurface seismic velocity profile based on earthquake infrasound signals recorded at airborne balloon platforms. The distributions of subsurface profiles inverted using data from 4 balloons (Fig. 5) are consistent with the Median Model, a median representation of seismic velocities in the Malay Archipelago from the literature. We also capture a crustal interface, consistent with the local Moho depth, with ± 6 km uncertainty. The Bayesian approach enables an examination of parameter trade-offs and distributions in the simultaneous estimation of source location and subsurface velocity.

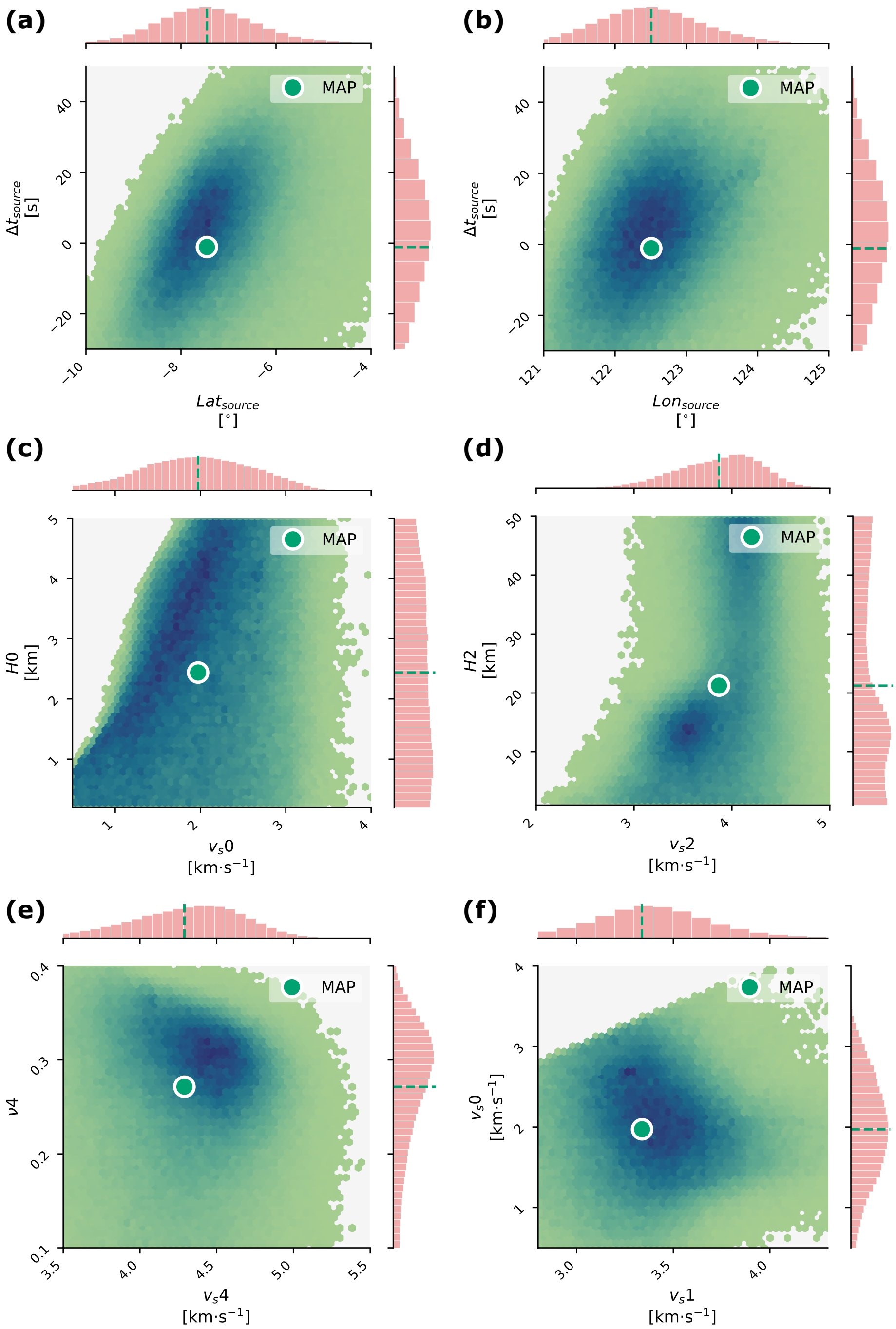

Fig. 6 Marginal probability density distributions resulting from the inversion of balloon data. Distributions of (a) origin time and latitude, (b) origin time and longitude, (c) first layer thickness and shear wave velocity, (d) third layer thickness and shear wave velocity, (e) Poisson's ratio and shear wave velocity in the fifth layer, and (f) shear wave velocities in the first and second layer. A darker hue represents a higher density of models.

We identify the main challenge of this balloon-based inversion as the reliable picking of seismic phases in single-component data. Besides the lack of waveform polarization estimation, balloon signals suffer from lower SNR on Earth at low frequencies due to buoyant motion through atmospheric perturbations and possibly from local turbulence induced by this motion (Gerier et al. 2024). Without knowledge of the source location, coda arrivals may also be misidentified: a broadband energy pulse from a wind burst or a secondary P-phase can be wrongly interpreted as an S-wave arrival, and higher-mode LR energy can obscure the fundamental mode at higher frequencies. These limitations could be mitigated in the future by improved signal processing methods, such as template matching or machine learning-based picking, as well as by additional instrumentation. Recent studies have proposed using Inertial Motion Units (IMUs) onboard balloons to better characterize pressure wave polarization (Bowman et al. 2022).

In conclusion, our findings confirm the viability of using balloons for seismic exploration. Our results strengthen the case for balloon seismology on Venus, as we demonstrated the ability to address challenges related to unknown sources and subsurface properties through a joint inversion using balloon infrasound data. Consequently, balloon seismology could provide valuable insights into the planet's current tectonic activity and internal structure. Additionally, balloons could gather seismic data in regions where surface deployment is challenging, such as the oceanic and polar areas of Earth.

4 Methods

4.1 Markov chain Monte Carlo inversion

Sophisticated Monte Carlo sampling approaches, such as Ensemble Sampling (Goodman and Weare 2010), Hamiltonian Monte Carlo (Neal 2011), or Parallel Tempering (Sambridge 2014), allow a thorough search through model space robust to the presence of multiple local minima.

Here, we choose the open-source implementation of an Ensemble Sampler in Python language named `emcee` (Foreman-Mackey et al. 2013) as the basis for our inversion framework. Its use here is motivated by its simplicity of application and its efficiency when sampling highly correlated parameter spaces, which could potentially be encountered in the hypocenter-velocity problem. Each McMC simulation is run for 10^6 iterations on an ensemble of 50 chains, resulting in a total of about 50×10^6 samples. The simulations are run with 32 CPUs on a high performance computing server.

4.2 Forward model and misfit

The inversion method is based on measurements of arrival times for different seismic wave types, namely P, S and LRs at a network of receivers. Considering a common and arbitrary reference time for the receivers and source of interest, the time of arrival of a wave W at receiver R can be written:

$$t_{W,R} = t_s + \Delta t_{W,R} + \Delta t_{air,R}, \tag{1}$$

where the earthquake occurs at time $t = t_s$ (s) since the reference time, W is the wave type among seismic or air-coupled P, S and LR, $\Delta t_{W,R}$ is the seismic travel time from the source to the piercing point at a ground station or below a floating balloon, and $\Delta t_{air,R}$ is the remaining travel time from the surface to the floating balloon, if applicable. For simplicity, we use the origin time of the Flores earthquake published by the USGS (03:20:23 UTC on 14 December 2021) as our reference time (International Seismological Center 2025). In the case of LRs, $\Delta t_{W,R}$ is frequency-dependent, allowing to model a range of arrival time measurements. At a specific receiver R, the travel time $\Delta t_{air,R}$ is independent of the phase type, and can be estimated knowing the balloon altitude and an atmospheric model at the time of the event. The recording of multiple phases W at several receiver locations provides a system of equations similar to Eq. 1.

Upon selection of a source location, origin time and subsurface model by the Monte Carlo sampling algorithm, the forward model is in charge of predicting the arrival time of waves at each of the station/balloons following Eq. 1. The travel times Δt_P and Δt_S of P and S waves are calculated using a ray-tracing method derived from the `LAUFZE` suite (Schweitzer 2012). This Fortran routine takes in a source-receiver distance and a layered subsurface model and in return predicts the arrival time of the fastest direct P and S body waves.

The travel times $\Delta t_{LR}(f)$ of LRs are calculated using a numpy-accelerated Python implementation of the `surf96` code (Herrmann 2013), called `disba` (Luu 2024). The code is given a layered subsurface model and outputs the group velocity $v_g(f)$ of the Rayleigh waves at the fundamental or higher modes. We obtain the travel time by the approximation:

$$\Delta t_{LR}(f) = \frac{d_s}{v_g(f)}, \tag{2}$$

where d_s is the epicentral distance, considering only the fundamental mode.

The travel time Δt_{air} from the ground to the balloon is calculated by integrating the vertical variation of sound speed $c_{air}(z)$ from $z = 0$ to the balloon altitude $z = z_b$:

$$\Delta t_{air} = \int_{z=0}^{z_b} \frac{\mathrm{d}z}{c_{air}(z)}. \tag{3}$$

Considering travel-time picks to have an uncorrelated Gaussian distribution with standard deviation σ (which is debatable, see e.g., Husen and Hardebeck (2010)), the log-likelihood function minimized by the Monte Carlo search is the sum of the following L2-norms:

$$\log P(\boldsymbol{d}|\boldsymbol{m}) = -\frac{1}{2} \sum_R \sum_i \frac{(t_{W_i,R}(\boldsymbol{m}) - t_{W_i,obs})^2}{\sigma^2_{W_i,R}}, \tag{4}$$

where W_i represents the available wave arrivals among $\{P, S, LR(f_i)\}$ and R are the available receivers.

4.3 Effects of balloon motion on arrival times

Contrary to a seismic station, a balloon is a non-stationary object, animated with a horizontal motion due to jet winds, and a oscillatory vertical motion due to buoyancy. Due to the horizontal balloon motion, the station-balloon distance is not constant over the duration of the earthquake signal and can impact Δt_W (see Eq 1). Assuming that the balloon is located at the distance d_0 from the source at time t_s, and that, in the worst-case scenario, it is moving with velocity v_b in the radial direction away or towards the source; and considering a homogeneous media of seismic velocity v_W for simplicity, the expression of Δt_W becomes:

$$\Delta t_W = \frac{d_0 + v_b \Delta t_W}{v_W}, \tag{5}$$

or

$$\Delta t_W = \left(\frac{1}{1 - v_b / v_W} \right) \frac{d_0}{v_W}. \tag{6}$$

Strateole2 balloons have a horizontal velocity of 5 to 8 m/s. This means a ~ 0.1 % change in travel time for P waves, and ~ 0.4 % for S and LR waves compared to a stationary receiver. This "balloon Doppler effect" can thus be neglected compared to other sources of errors in travel time estimations (Gerier et al. 2024).

In the same way, constant-volume balloons like the Strateole2 aerostat experience vertical motion, caused by wind perturbation. The stratification of the atmosphere, with density decreasing with altitude, exerts a restoring force through the volume of air displaced by the balloon. This leads to buoyancy oscillations, whose period depends on the Brunt–Väisälä pulsation N at the balloon equilibrium altitude, namely $2\pi f_0 = N = \sqrt{-\frac{d\rho}{dz}\frac{g}{\rho_e}}$, with g the constant of gravity and ρ_e the density at the balloon equilibrium altitude (Massman 1978). In the case of Strateole2 balloons, this oscillation has a period between 180 and 240 s and an amplitude of $10 - 100$ m, corresponding to about ~ 0.5 m/s. This speed is insufficient to produce any significant effect on arrival time or travel time estimations. However, it is responsible for a significant low-frequency noise in the balloon pressure recordings, as a variation of $10 - 100$ Pa is expected at each oscillation. Below, we describe a method we applied to mitigate this noise.

4.4 Inversion priors

Source location

We have considered here that we have no prior information on the epicenter location or source depth.Thus, we set uniform prior bounds of $[-90°, +90°]$ for lat_s and $[-180°, +180°]$ for lon_s. For the practical examples of this article, for which the epicenter is known *a priori* from earthquake catalogs, we simply restrict the starting latitudes and longitudes of the McMC chains to a range $\pm 20°$ closer to the known epicenter, so as to avoid stuck chains and speed up the computation. The source depth is also considered unknown, we thus chose [0,200] km as uniform prior bounds for h_s (see Extended Table A1).

Source origin time

The choice of prior bounds for the origin time is strongly dependent on the choice of reference time for arrival time picking. In the practical examples of this article, the chosen reference time is the USGS published origin time (International Seismological Center 2025), and we set prior bounds for t_s to $[-200, +200]$ s. In practice, a rough approximation of the origin time can be calculated by estimating the minimum and maximum possible source distance using prior bounds for seismic velocities, leading to ranges for t_s closer to thousands of seconds.

Layers and layer thickness

We have chosen here to parameterize our subsurface with a succession of homogeneous layers, as this parametrization is best adapted to the numerical methods (`disba`, `LAUFZE`) used in our forward model. The maximum source-receiver distance in our two inversions is about ~ 3000 km, a distance at which body waves have turning depths of ~ 600 km on Earth. It is therefore necessary to parameterize subsurface down to mantle depths.

In this study, the number of layers is fixed to 6, in addition to an underlying halfspace. Tests of the effect of the number of layers on the achieved misfit showed that the misfit does not significantly decrease for a higher number of layers (see the Supplementary Figure S8). The last layer and the halfspace are intended to represent upper-mantle velocities, hence having large prior thickness between 100 and 400 km. The uppermost layers represents a possible sedimentary region with thickness of 0.2 to 5 km. The remaining layers have intermediate prior thicknesses, allowing for variations within the crust, and can be found in Extended Table A1.

Seismic velocities and Poisson ratio

The inversion covers seismic velocities from the upper crust to the upper mantle. The thin top layer allows for possible sedimentary deposits and has prior bounds for v_s of $[0.5, 4]$ km/s. The following four layers correspond to crustal or upper mantle materials and have v_s within $[1, 6]$ to $[3, 6]$ km/s. The last layer and the halfspace are mantle layers with v_s within $[4, 7]$ km/s. v_p is calculated using the values of v_s and of the Poisson ratio ν. Prior bounds for ν are uniform within a range of $[0.1, 0.4]$ encompassing typical properties for crustal and mantle minerals (Christensen 1996). In addition to these uniform bounds for Poisson's ratio and shear wave velocity, we implement additional rules to restrict the acceptable prior models. Prior models must have no negative velocity gradient in the first 3 layers. Below that, negative changes in velocity are limited to $\Delta v_s, \Delta v_p < -1$ km/s. An upper limit of $v_p < 12$ km/s is set, which has an influence on the prior distribution of ν. The distribution of prior models can be found in the Supplementary Information (Fig. S9).

The density , to which P, S and LR travel times are less sensitive than seismic velocities, is not inverted but rather modeled using Birch's empirical law (Birch 1964).

4.5 Balloon noise correction

To improve the low-frequency SNR of the balloon pressure trace, the balloon buoyancy resonance (Massman 1978) is corrected following a method similar to Podglajen et al. (2022). The GPS altitude trace Z of each Strateole2 balloon is upsampled and interpolated to Z_{up}, so as to match the sampling rate of 1 Hz and exact timestamps of the pressure trace P, using a Hann taper in the frequency domain. Over small variations in altitude, the relation between pressure and altitude is quasi-linear. A sliding window of 500 s is run along the P and Z_{up} traces, and a linear regression is applied to determine the coefficients of their relation, valid for the center point of the window. These are then used to produce an auxiliary pressure trace P_{mod}, calculated from Z_{up}. Finally, the corrected pressure trace P_{corr} is obtained from $P_{corr} = P - P_{mod}$. The different traces and steps of the correction can be found in Extended Figure A1. This processing step helps partially correct the balloon buoyancy oscillations and improves subsequent frequency-time analysis.

4.6 Data processing and arrival picking

Key to the inversion framework is to properly identify and pick seismic arrival times. An infrasound signal is by nature single-component. Hence, classical techniques for separating P, S and LRs in 3-components seismic signals based on polarity cannot be used. Instead, we leverage other aspects of these arrivals, namely the impulsive nature of body waves and their envelopes and the dispersive nature of Rayleigh waves, distinguishable in the time-frequency domain.

To pick P and S wave, a two-step method is used. First, the signal is filtered in several frequency bands and its envelope is calculated using a Hilbert transform. For balloon signals, we use the envelope of the low-passed signal below 0.1 Hz, the high-passed signal above 0.05 Hz, and an intermediate signal band-passed between 0.03 and 0.1 Hz. For one-component seismic velocity signals, the signal is first low-passed or high passed at 1 Hz, or band-passed between 0.02 and 0.8 Hz. Part of the scattering in the envelopes is smoothed by calculating a sliding median over the 5, 10 and 20 s preceding each considered point in time. Using multiple sliding window sizes helps rule out picks in the envelope that could be due to a local scattered arrival. Using this envelope method, a first hypothesis on the arrival of P and S waves and their uncertainty can be made by identifying the start of the P and the S energy envelope. Then, in a second step, these picks are assessed in narrower frequency bands. We construct a filter bank by bandpass-filtering the single component signal in 10 narrow logarithmic intervals from ~ 0.001 Hz to the Nyquist frequency of the signal. This method present advantages for refining the P wave pick, more clearly visible at high frequency, and for confirming the S-wave pick, by identifying a later impulsive arrival spanning multiple intervals of frequency. Despite these two steps, the S wave arrival is only identified with a very large uncertainty in some cases.

To pick the Rayleigh Wave arrivals, we apply a Frequency-Time ANalysis (FTAN) to the single component signal using the Stockwell transform (also named S-transform), an approach analogous to a Morlet wavelet transform The LR is identified by its dispersion, and arrival times are picked at different frequencies around the maximum of the dispersed signal. Wavelet or S-transforms optimize the trade-off between time and frequency resolution in FTAN , but arrivals retain a frequency-dependent spread in time, which we interpret as our uncertainty in arrival time.

4.7 Post processing of inversion results

McMC inversions return a large amount of model parameter samples, out of which several statistically meaningful metrics should be extracted. In the Bayesian framework, we are interested in the most probable model given our data and prior, i.e., the model with the maximum posterior probability, referred to as MAP. Although a Monte Carlo inversion returns millions of samples, the curse of dimensionality means that the MAP is not necessarily among them. To determine an estimate of the MAP out of all our samples, we use the Mean-shift method, through which subset of 2×10^4 samples are migrated towards one or more regions of high density in the posterior space.

The MAP yields the region of high density throughout all dimensions. We are also interested in the behavior of individual or groups of parameters in lower dimensions. This is done by considering marginal distributions of parameters through histograms or density plots, as was done in the majority of figures throughout this article. In some cases, we apply additional processing to the marginal distribution in order to enhance visualization or enable easier interpretation. The marginal density distribution of subsurface parameters of Fig. 2 and 5 are obtained by dividing the counts of posterior model in each bin of the histogram by the mean count that would be obtained if all models had been uniformly distributed. A high value of Posterior/Mean count in these 2D representations thus means that there are significantly more models going through this area than in a uniform distribution.

We apply a similar process to interpret the distribution of layers in the posterior models. The posterior distribution of layer thickness can be transformed into a posterior distribution of interface depth using a cumulative summation starting from the top layer. However, comparing this distribution of interface depth to a uniform distribution, for example using a simple histogram, can be misleading, as the sum of uniform distribution from which the layer thicknesses were picked is not uniform itself. Here, we instead calculate the ratio of the number layer thicknesses counted in one bin in the posterior distribution, to the number predicted in a cumulative prior distribution.

For each layer N, the cumulative prior is defined as the cumulative posterior distribution of interface depths for $k < N$, summed with the prior distribution of thickness for layer N:

$$Prior(d_N) = \sum_{k=0}^{N-1} Posterior(h_k) + Prior(h_N), \tag{7}$$

where d_N is the depth of interface N. Mixing the prior and posterior distribution in this cumulative prior allows to rule out the effect of above layers on the distribution of lower layers. The final interface count ratio is obtained from $\sim 5 \cdot 10^5$ samples from the posterior and from each prior. An interface count ratio superior to one thus means that there is a higher probability that an interface is located at this depth, than what would be expected from a cumulated prior distribution.

Supplementary information. A more detailed description of the seismic and infrasound data used in this study, information on preexisting subsurface models as well as additional inversion products are available in the Supplementary Material.

Acknowledgements. The codes developed for this study makes use of open-source modules for seismology and McMC inversions, such as ObsPy (https://docs.obspy.org/) and emcee (https://emcee.readthedocs.io/en/stable/). We thank their contributors for providing and maintaining them.

Declarations

Funding. This work received support from the *Airborne Inversion of Rayleigh wave* (AIR) project, funded by the Research Council of Norway basic research program FRIPRO, Contract 335903, as well as NORSAR institute funding.

Conflict of interest/Competing interests. The authors declare no conflict of interest or competing interest in the writing of this article.

Ethics approval and consent to participate. Not applicable.

Consent for publication. All authors have consented to the publication of this manuscript.

Data availability. Seismic and ground infrasound data is retrieved from the International Federation of Digital Seismograph Networks (FDSN) (GEOFON: http://geofon.gfz-potsdam.de/doi/network/GE, Australian National Seismograph Network http://pid.geoscience.gov.au/dataset/ga/144675, Global Seismograph Network: https://www.fdsn.org/networks/detail/IU/) The Strateole2 TSEN data is available at https://doi.org/10.14768/c417e612-015d-4812-9b59-294a6570c7c3.

Materials availability. Not applicable.

Code availability. The data analysis and inversion software developed for this study was written in the Python and Fortran languages. It is available at https://github.com/m-froment/balloon-inv.

Author contribution. Conceptualization: MF, QB, SPN. Methodology: MF, QB, SPN. Software: MF, QB, JS. Validation: MF, Formal Analysis: MF, Investigation: MF, QB, SPN, JS. Data Curation: MF, QB. Writing - Original Draft: MF. Writing-Review and Editing: MF, QB, SPN, JS. Visualization: MF. Supervision: QB, SPN. Project Administration: QB. Funding acquisition: QB.

Appendix A Extended Data

Table A1 Extended Table: Prior limits for the inversion parameters.

Parameter	Unit	Minimum	Maximum
Source			
t_s	[s]	-200	200
Lat_s	[deg °]	-90	90
Lon_s	[deg °]	-180	180
h_s	[km]	1	200
Shear wave velocity			
v_{s0}	[km/s]	0.5	4
v_{s1}	[km/s]	1	6
$v_{s\{2-3\}}$	[km/s]	2	6
v_{s4}	[km/s]	3	6
$v_{s\{5-6\}}$	[km/s]	4	7
Layer thickness			
h_{l0}	[km]	0.2	5
h_{l1}	[km]	1	30
h_{l2}	[km]	1	50
h_{l3}	[km]	1	100
$h_{l\{4-5\}}$	[km]	100	400
Poisson's ratio			
$\nu_{s\{0-6\}}$	-	0.1	0.4

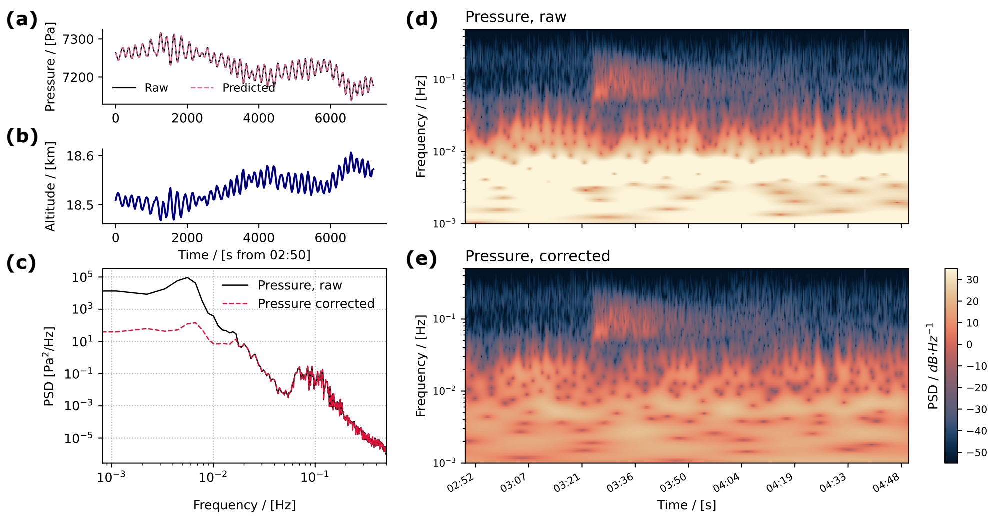

Fig. A1 Extended Figure: Correction of the vertical buoyancy oscillation in the Strateole2 data, illustrated for Balloon TTL3-17. Panel (a) shows the raw and predicted pressure time series, and panel (b) the upsampled GPS altitude trace used for the prediction. The power spectra (c) and wavelet spectrograms of raw (d) and processed (e) pressure signals show a clear reduction in buoyancy noise below 0.02 Hz.

References

Arrowsmith S, Park J, Che IY, et al (2020) Event location with sparse data: When probabilistic global search is important. Seismological Research Letters 92(2A):976–985. https://doi.org/10.1785/0220200292

Averbuch G, Houston R, Petculescu A (2023) Seismo-acoustic coupling in the deep atmosphere of Venus. The Journal of the Acoustical Society of America 153(3):1802–1810. https://doi.org/10.1121/10.0017428

Banerdt WB, Smrekar SE, Banfield D, et al (2020) Initial results from the InSight mission on Mars. Nature Geoscience 13(3):183–189. https://doi.org/10.1038/s41561-020-0544-y

Bellemare MG, Candido S, Castro PS, et al (2020) Autonomous navigation of stratospheric balloons using reinforcement learning. Nature 588(7836):77–82. https://doi.org/10.1038/s41586-020-2939-8

Berg EM, Lin FC, Allam A, et al (2020) Shear velocity model of Alaska via joint inversion of Rayleigh wave ellipticity, phase velocities, and receiver functions across the Alaska Transportable Array. Journal of Geophysical Research: Solid Earth 125(2):e2019JB018582. https://doi.org/10.1029/2019JB018582

Birch F (1964) Density and composition of mantle and core. Journal of Geophysical Research (1896-1977) 69(20):4377–4388. https://doi.org/10.1029/JZ069i020p04377

Bowman DC, Rouse JW, Krishnamoorthy S, et al (2022) Infrasound direction of arrival determination using a balloon-borne aeroseismometer. JASA Express Letters 2(5):054001. https://doi.org/10.1121/10.0010378

Brissaud Q, Martin R, Garcia RF, et al (2017) Hybrid galerkin numerical modelling of elastodynamics and compressible navier–stokes couplings: applications to seismo-gravito acoustic waves. Geophysical Journal International 210(2):1047–1069. https://doi.org/10.1093/gji/ggx185

Brissaud Q, Krishnamoorthy S, Jackson JM, et al (2021) The first detection of an earthquake from a balloon using its acoustic signature. Geophysical Research Letters 48(12):e2021GL093013. https://doi.org/10.1029/2021GL093013

Christensen NI (1996) Poisson's ratio and crustal seismology. Journal of Geophysical Research: Solid Earth 101(B2):3139–3156. https://doi.org/10.1029/95JB03446

Didion A, Komjathy A, Sutin B, et al (2018) Remote sensing of venusian seismic activity with a small spacecraft, the VAMOS mission concept. In: 2018 IEEE Aerospace Conference, pp 1–14, https://doi.org/10.1109/AERO.2018.8396447

Dziewonski AM, Anderson DL (1981) Preliminary reference Earth model. Physics of the Earth and Planetary Interiors 25(4):297–356. https://doi.org/10.1016/0031-9201(81)90046-7

Foreman-Mackey D, Hogg DW, Lang D, et al (2013) Emcee: The MCMC hammer. Publications of the Astronomical Society of the Pacific 125(925):306–312. https://doi.org/10.1086/670067, arXiv:1202.3665

Garcia RF, Martire L, Chaigneau Y, et al (2021) An active source seismo-acoustic experiment using tethered balloons to validate instrument concepts and modelling tools for atmospheric seismology. Geophysical Journal International 225(1):186–199. https://doi.org/10.1093/gji/ggaa589

Garcia RF, Klotz A, Hertzog A, et al (2022) Infrasound from large earthquakes recorded on a network of balloons in the stratosphere. Geophysical Research Letters 49(15):e2022GL098844. https://doi.org/10.1029/2022GL098844

Garcia RF, van Zelst I, Kawamura T, et al (2024) Seismic wave detectability on Venus using ground deformation sensors, infrasound sensors on balloons and airglow imagers. Earth and Space Science 11(11):e2024EA003670. https://doi.org/10.1029/2024EA003670

Gerier S, Garcia RF, Martin R, et al (2024) Forward modeling of quake's infrasound recorded in the stratosphere on board balloon platforms. Earth, Planets and Space 76(1):87. https://doi.org/10.1186/s40623-024-02030-7

Goodman J, Weare J (2010) Ensemble samplers with affine invariance. Communications in Applied Mathematics and Computational Science 5(1):65–80. https://doi.org/10.2140/camcos.2010.5.65

Haase J, Alexander M, Hertzog A, et al (2018) Around the world in 84 days. Eos URL http://eos.org/science-updates/around-the-world-in-84-days

Helffrich G (2000) Topography of the transition zone seismic discontinuities. Reviews of Geophysics 38(1):141–158. https://doi.org/10.1029/1999RG000060

Herrmann RB (2013) Computer programs in seismology: An evolving tool for instruction and research. Seismological Research Letters 84(6):1081–1088. https://doi.org/10.1785/0220110096

Husen S, Hardebeck J (2010) Earthquake location accuracy. Community Online Resource for Statistical Seismicity Analysis https://doi.org/10.5078/corssa-55815573

International Seismological Center (2025) On-Line Bulletin. https://doi.org/10.31905/D808B830

Kennett BLN, Engdahl ER (1991) Traveltimes for global earthquake location and phase identification. Geophysical Journal International 105(2):429–465. https://doi.org/10.1111/j.1365-246X.1991.tb06724.x

Krishnamoorthy S, Komjathy A, Pauken MT, et al (2018) Detection of artificially generated seismic signals using balloon-borne infrasound sensors. Geophysical Research Letters 45(8):3393–3403. https://doi.org/10.1002/2018GL077481

Krishnamoorthy S, Lai VH, Komjathy A, et al (2019) Aerial seismology using balloon-based barometers. IEEE Transactions on Geoscience and Remote Sensing 57(12):10191–10201. https://doi.org/10.1109/TGRS.2019.2931831

Kustowski B, Ekström G, Dziewoński AM (2008) Anisotropic shear-wave velocity structure of the Earth's mantle: A global model. Journal of Geophysical Research: Solid Earth 113(B6). https://doi.org/10.1029/2007JB005169

Laske G, Masters G, Ma Z, et al (2013) Update on CRUST1.0 - A 1-degree Global Model of Earth's Crust. In: EGU General Assembly, pp EGU2013–2658

Latham G, Ewing M, Press F, et al (1969) The Apollo passive seismic experiment. Science 165(3890):241–250. https://doi.org/10.1126/science.165.3890.241

Linkin VM, Kerzhanovich VV, Lipatov AN, et al (1986) VEGA Balloon Dynamics and Vertical Winds in the Venus Middle Cloud Region. Science 231(4744):1417–1419. 1696346

Lognonné P, Johnson CL (2015) 10.03 - Planetary Seismology. In: Schubert G (ed) Treatise on Geophysics (Second Edition). Elsevier, Oxford, p 65–120, https://doi.org/10.1016/B978-0-444-53802-4.00167-6

Lorenz RD, Panning M, Stahler S, et al (2019) Titan Seismology with Dragonfly: Probing the Internal Structure of the Most Accessible Ocean World. In: 50th Lunar and Planetary Science Conference, The Woodlands, Texas, p 2173

Lorenz RD, Shiraishi H, Panning M, et al (2021) Wind and surface roughness considerations for seismic instrumentation on a relocatable lander for Titan. Planetary and Space Science 206:105320. https://doi.org/10.1016/j.pss.2021.105320

Luu K (2024) Disba: Numba-accelerated computation of surface wave dispersion. Zenodo, https://doi.org/10.5281/zenodo.14534395

Macpherson KA, Fee D, Coffey JR, et al (2023) Using Local Infrasound to Estimate Seismic Velocity and Earthquake Magnitudes. Bulletin of the Seismological Society of America 113(4):1434–1456. https://doi.org/10.1785/0120220237

Massman WJ (1978) On the Nature of Vertical Oscillations of Constant Volume Balloons. Journal of Applied Meteorology (1962-1982) 17(9):1351–1356. 26178848

Mutschlecner JP, Whitaker RW (2005) Infrasound from earthquakes. Journal of Geophysical Research: Atmospheres 110(D1). https://doi.org/10.1029/2004JD005067

Neal RM (2011) MCMC Using Hamiltonian Dynamics. In: Handbook of Markov Chain Monte Carlo. Chapman and Hall/CRC

Panning MP, Lorenz R, Shiraishi H, et al (2020) Seismology on Titan: A seismic signal and noise budget in preparation for Dragonfly. In: SEG International Exposition and Annual Meeting. OnePetro, https://doi.org/10.1190/segam2020-3426937.1

Podglajen A, Le Pichon A, Garcia RF, et al (2022) Stratospheric Balloon Observations of Infrasound Waves From the 15 January 2022 Hunga Eruption, Tonga. Geophysical Research Letters 49(19):e2022GL100833. https://doi.org/10.1029/2022GL100833

Rolf T, Weller M, Gülcher A, et al (2022) Dynamics and Evolution of Venus' Mantle Through Time. Space Science Reviews 218(8):1–51. https://doi.org/10.1007/s11214-022-00937-9

Sambridge M (2014) A parallel tempering algorithm for probabilistic sampling and multimodal optimization. Geophysical Journal International 196(1):357–374. https://doi.org/10.1093/gji/ggt342

Schuler TK, Bowman DC, Izraelevitz JS, et al (2022) Long duration flights in Venus' atmosphere using passive solar hot air balloons. Acta Astronautica 191:160–168. https://doi.org/10.1016/j.actaastro.2021.10.030

Schweitzer J (2012) LAUFZE / LAUFPS. In: New Manual of Seismological Observatory Practice 2 (NMSOP-2), bormann, p edn. Deutsches GeoForschungsZentrum GFZ, Potsdam, p 1–14, https://doi.org/10.2312/GFZ.NMSOP-2_PD_11.2

Simmons NA, Myers SC, Johannesson G, et al (2015) Evidence for long-lived subduction of an ancient tectonic plate beneath the southern Indian Ocean. Geophysical Research Letters 42(21):9270–9278. https://doi.org/10.1002/2015GL066237

Stevenson DJ, Cutts JA, Mimoun D, et al (2015) Probing the interior structure of Venus. https://resolver.caltech.edu/CaltechAUTHORS:20150727-150921873

Supendi P, Rawlinson N, Prayitno BS, et al (2022) The Kalaotoa Fault: A Newly Identified Fault that Generated the Mw 7.3 Flores Sea Earthquake. The Seismic Record 2(3):176–185. https://doi.org/10.1785/0320220015

Sutin BM, Cutts J, Didion AM, et al (2018) VAMOS: A SmallSat mission concept for remote sensing of Venusian seismic activity from orbit. In: Space Telescopes and

Instrumentation 2018: Optical, Infrared, and Millimeter Wave, vol 10698. SPIE, pp 1651–1670, https://doi.org/10.1117/12.2309439

Tarantola A (2005) Inverse Problem Theory and Methods for Model Parameter Estimation. Society for Industrial and Applied Mathematics, https://doi.org/10.1137/1.9780898717921

Thurber CH (1992) Hypocenter-velocity structure coupling in local earthquake tomography. Physics of the Earth and Planetary Interiors 75(1):55–62. https://doi.org/10.1016/0031-9201(92)90117-E

Tromp J (2020) Seismic wavefield imaging of Earth's interior across scales. Nature Reviews Earth & Environment 1(1):40–53. https://doi.org/10.1038/s43017-019-0003-8